TOPOLOGICAL DESCRIPTIONS OF GRAIN BOUNDARIES IN GRAPHENE

BY

EMIL ANNEVELINK

THESIS

Submitted in partial fulfillment of the requirements
for the degree of Master of Science in Mechanical Engineering
in the Graduate College of the
University of Illinois at Urbana-Champaign, 2018

Urbana, Illinois

Advisers:

Associate Professor Elif Ertekin
Professor Harley Johnson

ABSTRACT

Since 2004, when monolayer graphene was first experimentally isolated, proof-of-concept graphene devices have added new functionality to engineering devices. As these devices become geared toward commercial applications, the development of high-throughput manufacturing methods that produce consistent properties become necessary. Defect engineering provides a promising method to tune the properties of graphene. Grain boundaries made of 5-7 dislocations are the most prominent defect in graphene and have been shown to be responsible for variability in properties. Therefore, we analyze how to change the structure of graphene through control of grain boundary motion. We analyze grain boundary motion–accomplished by moving individual dislocations–through both topological and energetic considerations. We use each method to show the equivalence of displacement shift complete lattice dislocations and grain boundary kinks. We show that all grain boundary kinks have dislocation character by verifying that graphene grain boundaries can be modeled by the displacement shift complete lattice. This allows us to think of altering the type and structure of graphene grain boundaries using the linear elastic theory of dislocations to nucleate and propagate grain boundary kinks.

ACKNOWLEDGMENTS

I would like to express my gratitude to my two advisors Prof. Elif Ertekin and Prof. Harley Johnson who guided me through the research and writing process. Their patience and support over the past two years has kept me focused to accomplished the research contained in this thesis.

To my family and friends, I appreciate your interest in my research and the questions you ask. Your questions remind me of the reasons why I do research: to be able to understand what is unknown. Your questions allow me to explain my interest in materials and their properties, which are foundational to every engineering device.

To my God, I express gratitude in all the knowledge you have given me that allows me to study your creation and understand you better.

TABLE OF CONTENTS

CHAPTER 1

INTRODUCTION - 2D MATERIALS

Two dimensional (2D) materials are only a single layer thick. The first usage of 2D material properties was nearly 500 years ago through graphene's layered 3D counterpart, graphite. The highly anisotropic (strong in-plane, weak out-of-plane) behavior of graphite allowed the material to easily mark surfaces. This led to the development of graphite based writing utensils similar to those that are still commonly utilized today [1]. Some 450 years later, the layered structure of graphite was understood as being composed of repeating sheets of graphene. However, even though the structure was theorized and better understood, the single layer stability of 2D materials was discounted and study was limited until fifteen years ago when Novoselov *et al.* used mechanical exfoliation through the "scotch tape method" to show that many 2D crystals are stable in ambient conditions [2]. Their major breakthrough was to use optical imaging on oxidized silicon as a processing step to reduce the regions where atomic force microscopy was used to confirm the single layer nature.

1.1 Structure

The experimental isolation allowed the structure of 2D materials to be analyzed, which confirmed theoretical predictions of their structure. 2D materials are characterized by strong in-plane bonding and weak (vdW) out-of-plane bonding. The in-plane bonding is covalent in character and utilizes all valence electrons of the constituent atoms such that there are no dangling bonds at the surface. Out-of-plane bonding is therefore weak and based on electrostatic interaction. The structure of 2D materials is highlighted in Fig. 1.1, where in-plane bonding networks are shown by cylinders connecting spherical atoms. The individual layers are shown to be stacked on top of each

other. The electrostatic attraction that hold the layered structures together is not shown.

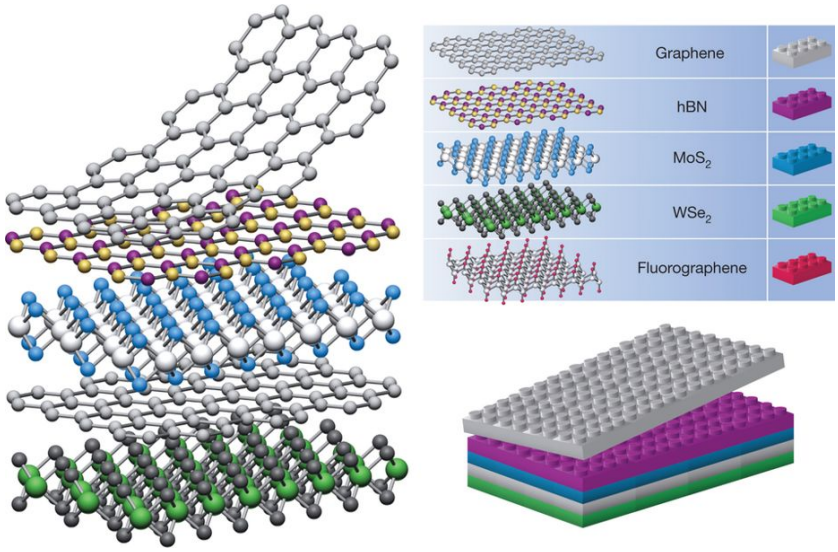

Figure 1.1: The structure of 2D materials, reproduced from Geim *et al.* [3]. The bonding network of different 2D materials is shown. In plane bonds are drawn connecting the atomic units of each material, while the out-of-plane bonds are not shown.

1.2 Types

2D materials are broadly classified by their atomic thickness and in-plane bonding network. Underneath this umbrella, there are three main types classified according to: "Graphene Family", "2D Chalcogenides", and "2D Oxides" [3]. Fig. 1.2 catalogs many 2D materials into a compact table based on these classifications. The graphene family is characterized by the well-known hexagonal bonding network of graphene. 2D chalcogenides are characterized as containing a transition metal and a chalcogen other than oxygen, which would classify it as a 2D Oxide. The 2D oxides have much in common with the chalcogens but also comprise perovskite and mica-type crystals. The most common materials in Fig. 1.2 are those that are stable in air (shaded in blue). Processing in inert environments has allowed less atmospherically stable materials (green, pink) to be studied. The schematic, therefore, sheds light on the challenges 2D materials present for future processing and device

manufacturing. However, the ever expanding list of predicted 2D materials (gray) shows the rich assortment of different structures and properties available that can be used in future devices.

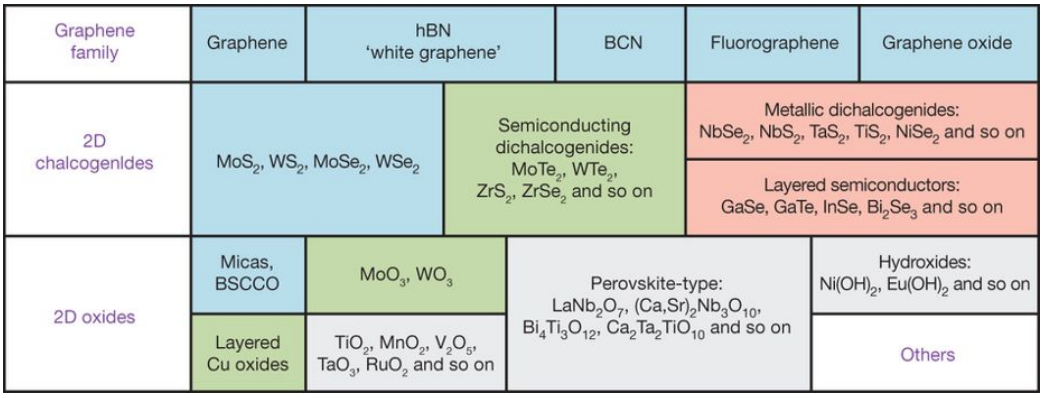

Figure 1.2: A catalog of 2D materials separated into three families from Geim *et al.* [3]. Blue shading shows stable monolayers. Green represents those probably stable in air, while those that are unstable in air but that may be stable in inert atmospheres are shaded pink. Gray shading indicates 3D compounds that have been successfully exfoliated down to monolayers but little more is known.

1.3 Applications

Many applications of 2D materials take advantage of the 2D structure by either stacking layers or utilizing the high surface area. The single layer structure is a 2D quantum well that makes the isolated layers have different properties from their 3D counterparts. The degree of confinement can be tuned based on how a material is stacked, eventually recovering their 3D properties [3, 4]. For example, the band gap of MoS_2 has been shown to vary based on the numbers of layers [5]. The ability to modulate band gaps through quantum confinement allows for design flexibility, which is increased even further when different materials can be stacked. Stacked devices have shown promise in nano-electronics and transistors [6].

The high surface area to volume ratio (SA/V) of 2D structures can also be used. Chemical reactions benefit from high SA/V ratios because there are more reactive sites. This property has been used in Li-ion batteries where graphite has been used as a lithium intercalant [7]. 2D materials improve

graphite anodes by making them even more porous and fatigue resistant. Structures based on 2D materials can increase the effectiveness of electrodes in batteries, fuel cells, gas generation, and sensing applications [8].

CHAPTER 2

GRAPHENE

We start by looking at graphene because it has the largest body of experimental work to draw from. We use previous work to understand how defects alter the atomic and electronic structure of graphene as a foundation for how defects could be used to engineer 2D materials. However, we must first understand the atomic and electronic structure of graphene before we can understand how defects alter them.

2.1 Atomic Structure

The atomic structure of graphene consists of sp2 hybridized carbon atoms each covalently bonded to three nearest neighbors. The three-fold coordination combined with 120° bond angles produces the hexagonal structure of graphene. Geometrically, this can be reduced to a triangular lattice with a two atom basis and lattice constant 2.46 Å where the carbon-carbon spacing is 1.42 Å. The lattice is shown from the perpendicular ([001]) direction in Fig. 2.1 to show the atomic structure, where the sub-lattices are different colors; the lattice vectors and carbon-carbon spacing are also shown. The last of carbon's four valence electrons (three are sp2-hybridized) is equally shared in a pi-bond with its nearest neighbors. The pi-bonds stabilize the 2D structure of graphene and keep it nominally flat, although when it is freestanding it vibrates out-of-plane due to thermal excitation [9].

2.2 Electronic Structure

The electronic structure of graphene is based on its four valence electrons that form three sigma bonds and one pi-bond. Fig. 2.2 shows the highest valence band and lowest conduction band of graphene for an extended zone

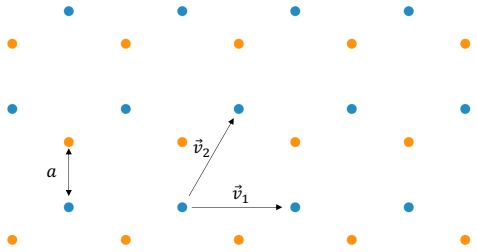

Figure 2.1: Atomic structure of graphene. The different colors denote the sub-lattices of the two atom basis of the triangular lattice that defines the structure of graphene.

in a rectangular coordinate frame. The inset of Fig. 2.2 shows a unique aspect of the electronic structure of graphene, the linear dispersion around the K-point with zero band gap. The linear dispersion is the result of 2D dirac fermions and implies that they are governed by Dirac's (relativistic) equation [10]. The fermions mimic charge carriers with zero effective rest mass and an effective speed of light. This makes graphene useful in accessing the physics of 2D dirac fermions and lead it to have fractional landau levels, micro-meter ballistic electron transport, and superconductivity, which can all be used to make devices [11, 12, 13].

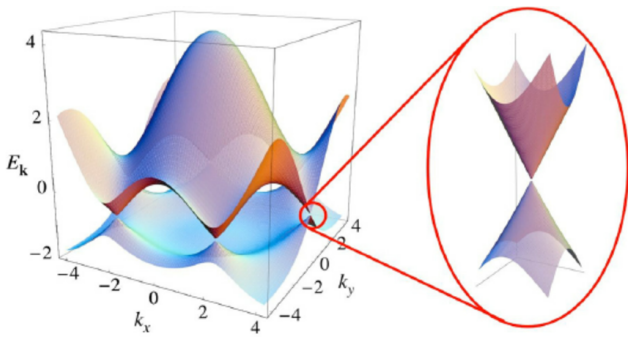

Figure 2.2: Band structure of graphene. The inset shows the linear dispersion around the K-point used from Maffucci *et al.* [14].

2.3 Properties and Applications

The atomic and electronic structure of graphene yield novel properties that have led to many predicted devices, some of which have been investigated and fabricated. A few of these applications are highlighted to show the breadth of graphene.

Graphene has been shown to have some mechanical properties that surpass those of any other engineering material. Graphene has a 2D elastic modulus of 300N/m, which when converted to 3D using the graphite layer separation, is about 5 times larger than that of steel, one of the most common engineering material [15]. The high strength of graphene makes it a useful additive in composite materials. Specifically, when graphene is added to aerogels, it gives the composite material a super-elastic behavior with low fatigue [16]. This strength can be combined with its high conductivity to make electrodes for electronics, batteries, and solar cells. For example, the super-elastic aerogel composite has applications as battery electrodes that are cycled thousands of times, where each cycle has a 3x volumetric expansion, which benefits from the super-elastic behavior. To act as a solar cell electrode, it must be transparent. Although graphene has a low band gap, which is normally associated with a high absorbance, it does not absorb much due to its single layer nature [17]. This has allowed graphene to be used as a top-electrode in experimental quantum dot solar cells [18]. Transparent electrodes are also useful as electronics displays. Graphene sheets have been manufactured into fully-functional touch-screen displays [19].

CHAPTER 3

PRINCIPAL DEFECTS IN GRAPHENE

Unfortunately, large-area, defect-free graphene is hard to obtain. The variable structure leads to variable properties that limit the device applications of the material. The quality of graphene is highly dependent on the production methods. The main production methods are mechanical or chemical exfoliation or chemical deposition. Exfoliation produces the highest quality graphene, where individual sheets are separated from graphite crystals, as in the original scotch tape method. This graphene is the basis for creating devices as the atomic structure is more controlled. However, the process of exfoliating graphene, either mechanically or chemically, is difficult to scale beyond the laboratory. Chemical vapor deposition is fundamentally different from exfoliation due to deposition of carbon, growing graphene as opposed to separating graphene from graphite. Chemical growth of graphene has the potential to be configured into a roll-to-roll process, which is an industry standard. To date, graphene has been grown to lengths of up to 100m using a roll-to-roll process [20].

One important drawback of growing graphene is that there are multiple nucleation points and, therefore, multiple graphene domains separated by defects. The intersections of these domains are places of misregistry between grains, and grain boundaries are present to facilitate the transition between the two. These grain boundaries are the basis for variable properties of chemically grown graphene. For example, grain boundaries have been shown to alter the fracture strength by a factor of three and the electronic conductivity by an order of magnitude [21, 22]. Therefore, insight into the formation and propagation of grain boundaries is important in order to engineer the structure of graphene allowing for better control over properties.

3.1 Dislocations

Defects in graphene are changes in the local arrangements of carbon atoms. They are characterized by the number of carbon atoms in an atomic ring. The most common defects in graphene, 5-atom and 7-atom rings, can be interpreted as disclinations. Disclinations violate the rotational symmetry of a crystal and are classified as either positive (>6 atom ring) or negative (<6 atom ring). Isolated disclinations are not typically found in materials due to the long-range elastic effect of breaking rotational symmetry. Instead, disclinations are often paired to cancel some of the long-range elastic effects (e.g. positive and negative disclinations of the same magnitude). However, the discreteness of the atomic lattice prevents the disclinations from being superimposed and therefore cannot remove all long-range elastic fields from the system. The residual long-range elastic strain field is centered at the disclinations, where the discrete separation and the magnitude of paired disclinations add a certain number of half-planes to the lattice.

In 3D materials, dislocations are defects that add a half-plane of atoms to a lattice. So, a pair of disclinations in graphene is a dislocation, where the dislocation core is defined by the disclinations present and the beginning of the half-plane of atoms. We classify defects in 2D materials using the same terminology where the Burgers vector corresponds to the strength of a dislocation based on the number of half-planes that are added.

3.1.1 Dislocations in Graphene

There are many dislocation variants in graphene depending on the pairing of disclinations in the core [23]. It is common to define the dislocation core structure of graphene according to the types of disclinations present and their spacing [24]. Experimental observations have shown disclinations with four to eight carbon atoms with spacings of up to two lattice vectors. However, since the dislocations have disclinations that are adjacent to one another the spacing is often omitted.

The Burgers vector of a dislocation is dependent on the types of disclinations and their spacing. The most common dislocation is a pair of disclinations with 5-atom and 7-atom carbon rings that share an edge. Fig. 3.1 marks each ring with a black or white triangle to represent the positive or

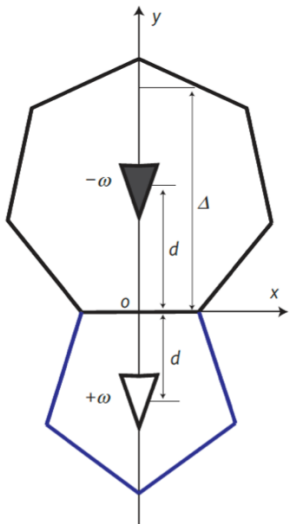

Figure 3.1: Schematic of a disclination dipole that makes an edge dislocation. Reproduced from [21]. The filled triangle marks the center of the positive disclination while the unfilled triangle marks the center of the negative disclination. The disclinations share an edge and have spacing d, which is approximately one lattice vector.

negative disclination respectively. Together, these disclinations form a dislocation whose Burgers vector is equal to a single lattice vector due to the addition of a single half-plane of lattice points [21]. This dislocation will be referred to as an edge dislocation.

3.2 Dislocation Networks and Grain Boundaries

Just as a pair of disclinations combine to form a dislocation that reduces the long-range elastic strain, networks of dislocations can reduce their long-range elastic strain fields. Just like disclinations, the strain fields of dislocations can cancel if oppositely oriented dislocations are close to one another. Stone-Wales and flower defects are examples of dislocation networks that have dislocations whose elastic strain fields partially cancel [25, 26].

However, there are also networks of similar-oriented dislocations whose Burgers vectors combine together to reduce the long-range elastic strain through a global change, normally a rotation, in the atomic structure. The dislocations condense and separate the crystal lattice into two regions that are related by a misorientation angle. The two separated regions are called

grains and their boundary is a condensed dislocation network referred to as a grain boundary.

Grain boundaries are classified using their misorientation and line angles. The misorientation angle θ_m is the angle that transforms the lattice vectors between two grains. The line angle θ_l corresponds to the direction of the boundary relative to the bisector of θ_m. Therefore, θ_l spans from -$\theta_m/2$ to $+\theta_m/2$ where a line angle of 0° corresponds to a symmetric boundary as it bisects the misorientation angle of the two grains. The drawback to using only θ_m and θ_l to classify grain boundaries is that they do not uniquely determine a grain boundary due to the degeneracy of dislocation networks that result in the same angles θ_m, θ_l. The only way to uniquely specify a grain boundary is to know all the dislocations that constitute it. Alternatively, the degeneracy can be lifted by assuming the type and orientation of dislocations present.

3.2.1 Graphene Grain Boundaries

The dislocation structure of grain boundaries has been analyzed experimentally and theoretically to obtain statistics on the types and orientations of dislocations. In the case of graphene, the atomic structure has been analyzed experimentally through high resolution transmission electron microscopy (HRTEM) and theoretically through kinetic Monte Carlo (KMC) simulations. Ophus *et al.* analyzed the HRTEM images from nearly nine hundred grain boundaries to asses the atomic structure [27]. Their work found that nearly all well-annealed grain boundaries are composed of 5-7 edge dislocations. The observed low angle boundaries contained isolated dislocations while high angle boundaries are composed of connected dislocations. Through simulation, Zhuang *et al.* annealed amorphous carbon using only bond rotations in KMC [28]. The results from Zhuang *et al.* show that as the simulation evolves, the grain boundary structure tends toward connected dislocations with line angles close to zero, *i.e.* parallel to the boundary. We can summarize these two results as grain boundaries having structures with edge dislocations whose (i) burgers vectors have like sign and (ii) directions are nearly parallel to the boundary. Using these two requirements, the misorientation and line angle of graphene grain boundaries now uniquely define

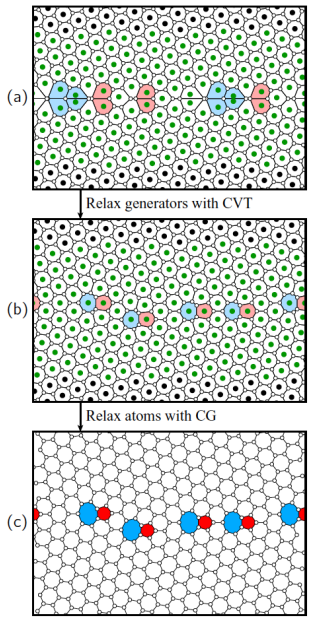

Figure 3.2: The steps of the CVT algorithm reproduced from Ophus *et al.* [27]. (a) The generators of a naive structure, which are minimized in (b) according to Lloyd's algorithm [29]. (c) The carbon atoms are relaxed using CG to produce graphene grain boundaries.

the grain boundary space.

Ophus *et al.* used these two assumptions about edge dislocations to develop an algorithm that constructs low-energy graphene grain boundaries that match experimentally annealed samples using only θ_m and θ_l [27]. Fig. 3.2 shows the three steps of the process, which uses centroidal voronoi tessellations (CVT) as a mediating step to find structures similar to experimentally annealed samples. In Fig. 3.2a, a triangular lattice is generated with the given θ_m and θ_l. The triangular lattice is the dual lattice of the carbon atoms, where the triangular lattice sites are the centroids (CVT generators) of the carbon atom locations. As can be seen in Fig. 3.2a, the initially proposed structure contains many unrealistic shapes at the boundary. So, the CVT generators near the boundary (green) are relaxed using Lloyd's algorithm while keeping the generators far from the boundary (black) fixed [29]. The relaxed structure in Fig. 3.2b removes the unphysical atomic rings and contains mostly hexagons with 5-7 edge dislocations that are parallel to the boundary. The carbon atoms are then relaxed using conjugate gradient (CG) minimization to produce the grain boundary structure in Fig. 3.2c.

Ophus *et al.* verified the grain boundary generation method by comparing

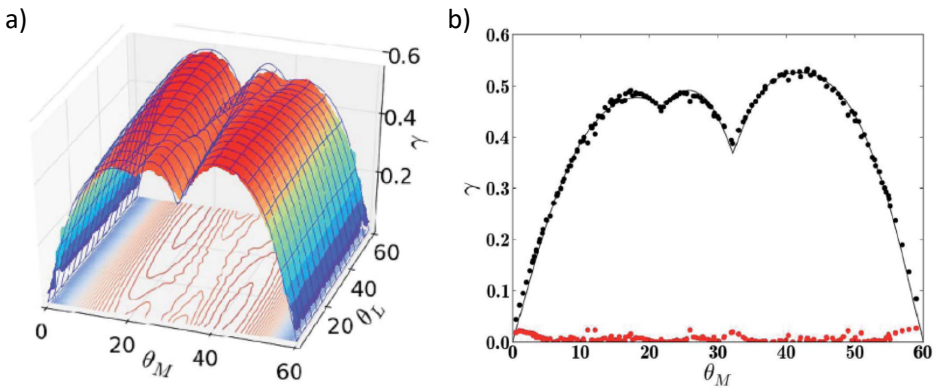

Figure 3.3: Configurational phase space of graphene grain boundaries reproduced from Shekhawat *et al.* [30]. (a) The full configurational phase space for θ_m and θ_l with a resolution of 0.5°. (b) The line energy for boundaries with θ_l=0° to highlight the cusps at 21.78° and 32.2°.

it to HRTEM images of the atomic structure. Nearly all of the experimental structures matched those of the generated structures. Therefore, the CVT based method can be assumed to accurately produce grain boundaries.

The CVT algorithm was used by Shekhawat *et al.* to find the grain boundary line energies of graphene for 4122 unique combinations of θ_m, θ_l [30]. The combinations are used to map out the grain boundary configurational phase space to find energy minima, or cusps, at geometrically favorable angles. The geometrically favorable angles correspond to global rotations that accommodate the strain from networks of edge dislocations with similar sign [31].

The phase space findings of Shekhawat *et al.* are reproduced in Fig. 3.3. Fig. 3.3a shows the line energies of the entire configurational space for all combinations of θ_m, θ_l, while Fig. 3.3b isolates the line energy for θ_l=0 to show the cusps at $\theta_m = 21.78°, 32.2°$. The $\theta_m = 21.78°$ and $\theta_m = 32.2°$ boundaries correspond to geometrically favorable angles as expected by 3D grain boundary theory [32]. Specifically, a misorientation close to θ_m=32.2° has been found through KMC by Zhuang *et al.* and later through Fourier analysis of polycrystalline samples by Tyurnina *et al.* to be present in annealed samples [28, 33].

CHAPTER 4

TOPOLOGICAL ANALYSIS FOR GRAPHENE GRAIN BOUNDARIES

We developed a topology-based method of analysis that aligns with the geometric concepts of lattices. We primarily use the coincident site lattice and displacement shift complete lattice to analyze grain boundary structure and their defects. By using topology, we draw from work that has been done on a variety of systems and expect that our work will be transferable to materials with different lattices allowing for graphene to serve as a foundation for other 2D materials.

4.1 Coincident Site Lattice

The Σ description of grain boundaries comes from the coincident site lattice (CSL), which was used in the 1970's to analyze and model grain boundaries as dichromatic patterns. Dichromatic patterns are, in essence, interference patterns made by superposing the lattices of neighboring grains. An example of a dichromatic pattern for two BCC lattices is seen in Fig. 4.1, where each lattice is shaded either white or black to highlight the difference in structure. A CSL is generated from the dichromatic pattern by looking at the interference sites, coincident sites, between the black and white lattices. Assuming there is at least one coincident point, the dichromatic pattern is a lattice of coincident points because the interfering points are part of lattices themselves. Therefore, only the primitive unit cell of a dichromatic pattern is shown in Fig. 4.1. Fig. 4.1 contains the primitive unit cell of a $\Sigma 33$ CSL of two BCC lattices. The Σ parameter is dependent on the orientations of the two grains and describes their periodicity. The Σ parameter is defined as the number of lattice points from each underlying lattice to the number of coincident points. It can also be defined in terms of the areas of the primitive unit cells of the CSL and underlying lattice as

$$\Sigma = \frac{\#\ lattice\ points}{\#\ CSL\ Points} = \frac{A_{CSL}}{A_{at}} \tag{4.1}$$

where A_{CSL} and A_{lat} correspond to the areas of the CSL and atomic lattices.

The CSL lattice spacing a_{CSL} and Σ determine the periodicity of a grain boundary, where a low Σ boundary corresponds to a small a_{CSL} and high Σ boundary corresponds to a large a_{CSL}. Using the principle that grain boundaries are networks of repeating dislocations, the periodicity of the lattice becomes a powerful tool to predict which grain boundaries are present. Generally, smaller period (low Σ) structures correspond to low-energy cusps in the configurational space because they allow for the efficient summing of the dislocation strain fields into global rotations [32]. Physically, this manifests as high angle grain boundaries in materials that contain evenly and densely spaced dislocations where the global rotations accommodate the extra half planes of edge dislocations.

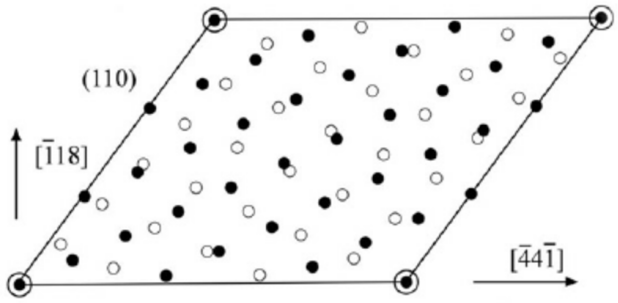

Figure 4.1: The dichromatic pattern of two misoriented bcc lattices reproduced from Mazilova *et al.* [34].

4.1.1 Coincident Site Lattice of Graphene Grain Boundaries

Although dichromatic patterns and CSLs were developed for 3D systems, they can be also be used for 2D systems like graphene. The interference pattern of a $\Sigma 7$ grain boundary in graphene is shown in Fig. 4.2. The dichromatic pattern shows only one of the triangular sublattices of graphene for each rotation to highlight the periodic structure of a $\Sigma 7$ boundary. In this image, it is easy to use Eq. 4.1 to find Σ for this dichromatic pattern.

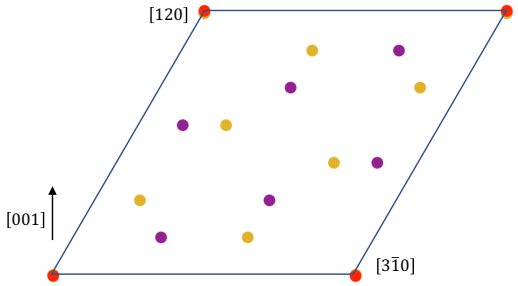

Figure 4.2: The dichromatic pattern for a Σ7 boundary in graphene. Purple and gold circles represent the sub-lattices of each grain in a grain boundary. The coincident points are at the vertices of the primitive unit cell in red.

4.1.2 Calculation of Σ

An analytic method, as opposed to post-processing of the dichromatic patterns, is needed to calculate Σ in order to create grain boundaries in materials. Unfortunately, there is no analytic relationship between Σ and θ_m because of the inherent discrete nature of lattices that make the relationship between θ_m and Σ discontinuous. The developed methods therefore use discrete mathematics that solve for Σ given the topological constraints of the underlying lattices. Warrington and Bufalini combined the geometric rules that govern the relationship between the lattice vectors and Σ into an algorithm to find Σ from θ_m and vice versa [35]. Their first derivation was done for cubic systems and is reproduced here.

A misorientation matrix R_{AB} is defined by the transform that takes lattice A to B. If this misorientation corresponds to a CSL, then R_{AB} can be expressed in terms of r_{AB} and Σ, where r_{AB} has the same shape as R_{AB}, but all its components and Σ are integers that satisfy

$$R_{AB} = \frac{r_{AB}}{\Sigma}. \tag{4.2}$$

This can be shown for a cubic crystal. The columns of R_{AB} must be of the form h/Σ, k/Σ, l/Σ where h, k, l correspond to the miller indices of the orientation of lattice B with respect to the coordinate system of lattice A. So, the columns of r_{AB} are made using the miller indices h, k, l, whose norm is Σ. A necessary condition for rotation is that $h^2+k^2+l^2 = \Sigma^2$. The length of all lattice vector must remain invariant under rotation. Even though this derivation is for cubic systems, it can be extended to any crystal system as

long as the correct norm is used to maintain the lengths of lattice vectors under rotation. Warrington extended this to hexagonal lattices like graphene in 1975 [36].

4.1.3 Usage of Σ transformation

We use this procedure to find the misorientation angles of naturally coincident grain boundaries like what is shown in Fig. 4.2. This uses the same procedure from Eq. 4.2, but a 2D hexagonal lattice is used instead of using a cubic lattice. The major difference is that the hexagonal norm is used to ensure a pure rotation. These coincident boundaries lend themselves nicely to the periodic boundary conditions often used in simulations. We can then use Σ to ensure that we look at low and high Σ boundaries to make sure that any properties we find for grain boundaries are not unique to the low strain grain boundaries found at the cusps in Fig. 3.3.

4.2 Displacement Shift Complete (DSC) Lattice

Experimental grain boundaries do not perfectly match the commensurate structures predicted by CSL theory. Instead, there are defects in the boundary, normally kinks, that shift the commensurate points to create grain boundaries with $\theta_l \neq 0$. The kinks are defects themselves and are called grain boundary dislocations, secondary dislocations, or displacement shift complete (DSC) dislocations [32]. These names all refer to the same feature which is not actually a dislocation in the sense that it does not correspond to an extra half-plane in either of the crystal lattices. However, these features are dislocations in (and add a half-plane to) the DSC lattice and account for shifts to the CSL points along the grain boundary.

The DSC lattice was developed to describe grain boundary defects in 3D materials though, as we will show here, it can be used in 2D materials as well. The DSC lattice has the same orientation as the CSL, but the CSL lattice vectors are a factor of Σ larger or, $\vec{a}_{CSL} = \Sigma\vec{a}_{DSC}$. The DSC lattice contains all the symmetry conserving translations of the CSL. The implications is that every lattice point of the two lattices of a CSL lattice contains a DSC lattice point [37]. However, as can be seen in Fig. 4.2, all the points of both

crystal lattices do not create a new lattice. Therefore, the DSC lattice is the coarsest lattice that contains all the lattice sites of each lattice. The empty sites enumerate the possible locations where lattice points may shift to create kinks. The ability to enumerate the possible shifts of a grain boundary make the DSC lattice a useful construction to analyze grain boundary kinks, *i.e.* grain boundaries with $\theta_l \neq 0$. Fig. 4.3 shows an example DSC lattice for a primitive unit cell of a $\Sigma 11$ CSL boundary for two FCC crystals about the [110] direction; the DSC lattice is drawn in as thin lines. The eleven grid lines can be easily counted across the unit cell in each direction. Each lattice point (the larger black and white circles) lies are on a DSC lattice point (intersection of two lines). If either lattice is shifted by a DSC lattice vector, the CSL is maintained but translated to a new location. Note, the smaller circles are the basis atoms of the FCC lattice and therefore are not on DSC lattice sites.

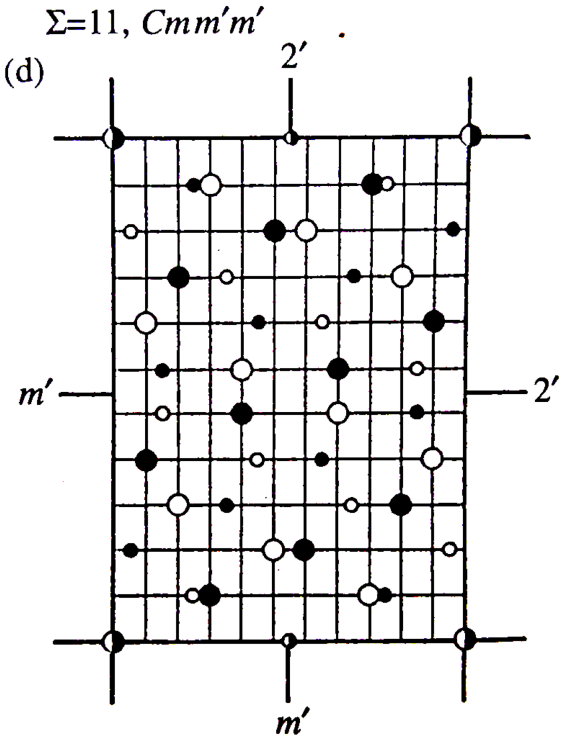

Figure 4.3: The $\Sigma 11$ dichromatic pattern of two FCC crystals with the DSC lattice in thin black lines reproduced from Pond *et al.* The larger circles correspond to the lattice points, while the smaller circles represent the basis atoms of the FCC crystal [38].

4.2.1 Example in Graphene

The DSC lattice for the Σ7 dichromatic pattern from Fig. 4.2 is produced in Fig. 4.4. Fig. 4.4 shows the DSC lattice in cyan superimposed on the dichromatic pattern made from the lattices of the two grains for a Σ7 boundary. As with the Σ11 FCC dichromatic pattern, it is easy to count the number of DSC points between the CSL vertices in red. Again, each of the sites of each atomic lattice corresponds to a DSC lattice site, and any shift of the atomic lattices to a different DSC lattice site shifts the CSL lattice.

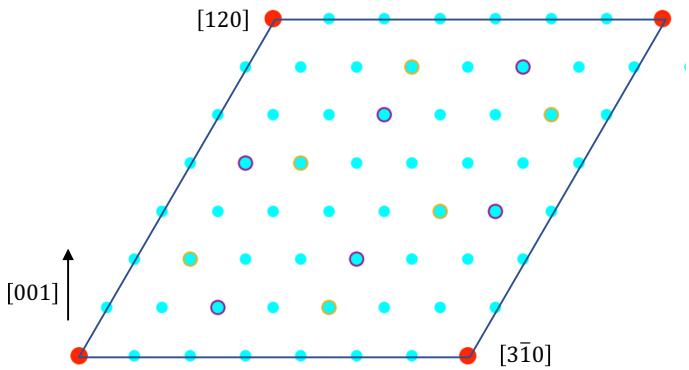

Figure 4.4: The dichromatic pattern (gold and purple) with a superimposed DSC lattice (cyan) for a Σ7 boundary in graphene. The CSL lattice is marked in red.

CHAPTER 5

GRAPHENE GRAIN BOUNDARY MOTION USING THE DSC LATTICE

We now transition to analyzing the motion of graphene grain boundaries at the atomistic level as dislocation networks and in the DSC framework as DSC dislocations. In this way, we will be able to analyze grain boundary motion through both lenses.

5.1 Kink Migration Mechanism

We start by constructing atomic scale models of grain boundaries with arbitrary θ_m using a modified version of the algorithm developed by Shekhawat *et al.* [30]. A unit cell is generated such that it contains two oppositely oriented grain boundaries with the smallest repeat distance. The minimum unit cell height is equivalent to the CSL spacing, a_{CSL}, for a particular θ_m. Each grain boundary unit cell contains one or two edge dislocations depending on the type of grain boundary (*e.g.* zig-zag or armchair) [21]. An example of a unit cell is seen in Fig. 5.1a. The unit cells are stacked to generate supercells of height H and width W, where the grain boundaries are evenly spaced $W/2$ apart. Instead of reporting H in Angstroms, we introduce $\bar{H}$, which is normalized by the unit cell height, a_{CSL}, so that it is dimensionless and represents the number of repeat units. The same is done for K to yield $\bar{K}$. For instance, Fig. 5.1a shows a supercell built by stacking six unit cells ($\bar{H}$ = 6), and Fig. 5.1b shows a magnified atomistic representation for the $\Sigma 7$ grain boundary.

We translate the boundary in our supercells by gliding the dislocations that compose the boundary. We consider grain boundary motion to be the result of the nucleation of double kinks in symmetric grain boundaries and the propagation of kinks until they annihilate with an oppositely oriented kink. Fig. 5.1c,d shows an intermediate step in the process where the kinks

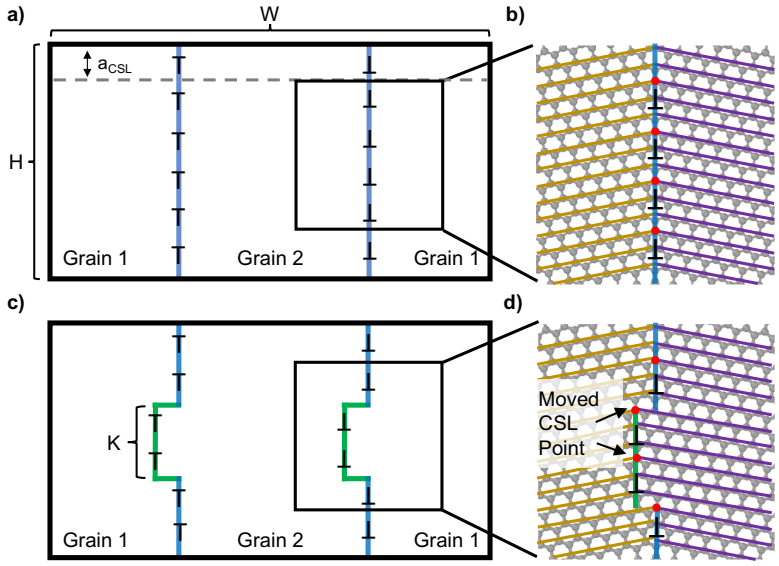

Figure 5.1: Schematic showing (a,b) straight and (c,d) kinked grain boundaries in graphene. (a,c) Schematic of a periodic supercell of height H and width W containing a pair of anti-parallel grain boundaries. The gray line in (a) marks the unit cell of a grain boundary whose height is the smallest repeat distance possible, a_{CSL}. In (c) a portion of the grain boundary (K units long) has migrated, corresponding to the formation of a double kink. (b,d) The corresponding atomic-scale structure for the case of a $\Sigma 7$ boundary. The grain orientation is indicated by gold/purple parallel lines. The migration of the grain boundary corresponds to a shift in the coincident site lattice (CSL) (red points) in the region where the migration has occurred.

are a distance $\bar{K}$=2 apart. Our process nucleates a double kink by gliding a dislocation through a bond rotation (Fig. 5.1 c,d). The kink then propagates by sequentially gliding adjacent edge dislocations, moving the kink sidewalls and causing the grain boundary to translate. As adjacent dislocations in the grain boundary glide, $\bar{K}$ increases to become equal to $\bar{H}$ at which point, the grain boundary has migrated by one dislocation Burgers vector. The gliding of a dislocation changes the location of registry between the grains (the coincident points of the CSL) to shift. The CSL shift is seen in Fig. 5.1b,d, where the glide of an edge dislocation moves the CSL (colored in red) by one dislocation Burgers vector.

5.2 Topological Equivalence of Grain Boundary Kinks and DSC Dislocation

We now the develop the understanding of grain boundary kinks in the DSC lattice. This is first done topologically and then energetically by comparing atomistic simulations of graphene and continuum simulations of DSC dislocations. The topological equivalence is shown through the equivalent movement of a CSL point by the glide of edge dislocations (Fig. 5.1) and the nucleation and propagation of a DSC dislocation dipole (Fig. 5.2). By associating the motion of CSL points with grain boundary motion, we formalize the DSC interpretation of grain boundary motion.

We show that DSC dislocations move CSL points by superimposing the DSC lattice for a $\Sigma 7$ boundary onto the lattices of the bicrystal in Fig. 5.2. We perform a shift to the coordinates of Lattices 1 and 2 and the DSC lattice from Fig. 5.2a such that the coordinates in the region between the gray lines of 5.2b are all shifted by a DSC lattice vector oriented vertically, parallel to the grain boundary and perpendicular to the gray lines. This shift vector is shown by the small black arrow below the lower gray line. The shift is equivalent to the nucleation of oppositely oriented dislocations in the DSC lattice centered at the symbol, Ð, and shown in the inset. The introduction of this shift to all points between the gray lines is equivalent to the introduction of two edge dislocations of opposite orientation in the DSC lattice. The DSC dislocations cause the CSL points (red) in the shifted region to translate by a lattice vector of either Lattice 1 or 2 (and notably not by the DSC vector that describes the shifts of Lattice 1, Lattice 2, and the DSC lattice). The shift in the CSL point caused by a DSC dislocation is the same as that associated with a grain boundary kink, and therefore effectively represents the presence of a kink in the grain boundary.

5.3 Energetic Equivalence of Grain Boundary Kinks and DSC Dislocations

We supplement the topological equivalence between grain boundary kinks and DSC dislocations by finding the migration energies of grain boundaries at both the atomistic and DSC levels.

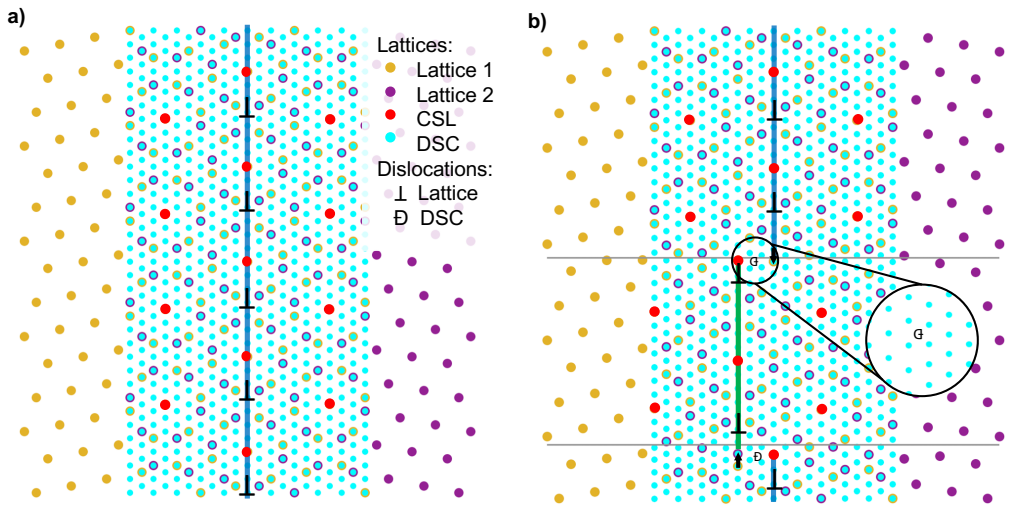

Figure 5.2: Schematic showing the equivalence of a grain boundary kink to a dislocation in the displacement shift complete (DSC) lattice. (a) Straight and (b) kinked grain boundary showing arrangement of gold and purple lattice points to the left and right of the boundary respectively. Red points indicate the CSL, which represents the lattice points shared by both grains. Teal points indicate the DSC lattice. The DSC lattice is constructed so that it contains all of the lattice points of both lattices, which means most DSC lattice sites are empty. In (b), kinks in the grain boundary corresponds to a region (between the gray lines) where the CSL is shifted. The shift in the CSL can also be understood as dislocations in the DSC lattice, with the Burgers vector of the dislocation indicated by black arrows. The inset isolates the DSC lattice to highlight the dislocation core where there is an extra half-line of lattice points.

5.3.1 Atomistic Simulation

The atomistic simulations utilize supercells of varying height, $\bar{H}$, and width, W. They are created using the modified algorithm that produced Fig. 5.1, where each supercell contains two anti-parallel Σ grain boundaries separated by $W/2$. Due to the use of periodic boundary conditions, this amounts to modeling an infinite array of parallel grain boundaries of alternating direction. Fig. 5.1b shows the atomic structure of the grain boundary with the 5-7 dislocations. The total energies of atomic configurations are determined using LAMMPS [39]; we use the Tersoff interatomic potential parameterized by Broido *et al.* to describe interactions between carbon atoms [40, 41].

Since our atomistic simulations invoke periodic boundary conditions, the energy of kink formation and propagation may be influenced by image inter-

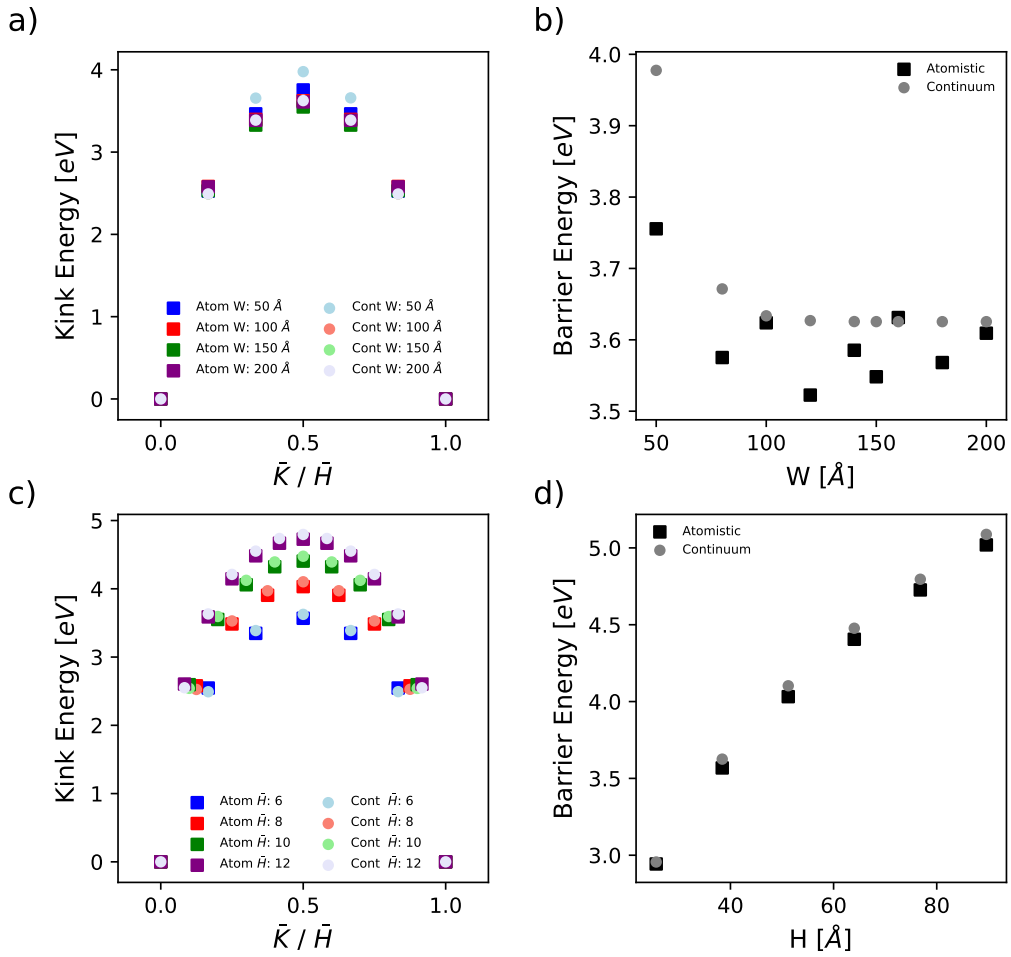

Figure 5.3: The effect of simulation cell size on the migration energy for the $\Sigma 7$ boundary. (a, b) shows the effect of changing the super cell width (W) while keeping $\bar{H}$ constant at 6 CSL periods. (a) shows the full energy profile for four different super cell widths. To highlight the dependence of the barrier energy on super cell width, (b) isolates the migration barrier energy for a range of super cell widths. When the cell width is greater than 100 Å the interaction energy plateaus, so the contribution from the anti-parallel grain boundary is negligible. This is compared to the effect of changing the super cell height, reported as the number of CSL periods $\bar{H}$, while keeping the width constant at 180 Å. (c) shows the full energy profile for four super cell heights and (d) isolates the migration barrier energy for a range of super cell heights. The logarithm of H is plotted instead of $\bar{H}$ to give units to the dependence of the barrier energy on H.

actions from neighboring supercells. To assess the magnitude of finite size effects, we present the effect of supercell parameters (W, $\bar{H}$) on the energy profile for a $\Sigma 7$ boundary. Fig. 5.3a,b considers how the grain boundary

migration barrier varies for different W for fixed $\bar{H} = 6$, and Fig. 5.3c,d considers how the grain boundary migration barrier varies for different $\bar{H}$ for fixed W=180 Å. The energy profiles in Fig. 5.3a,c show the nucleation and propagation of a double kink in a grain boundary. The kink energy is shown *vs.* $\bar{K}/\bar{H}$ relative to that of the unkinked grain boundaries at $\bar{K}/\bar{H} = 0$. The migration energy is symmetric across the position $\bar{K}/\bar{H} = 0.5$ due to the periodic boundary conditions and translational symmetry of the grain boundaries. The maximum occurs at $\bar{K}/\bar{H} = 0.5$, which corresponds to the point where exactly half of the grain boundary has migrated. This energy is classified as the *barrier energy* for grain boundary motion. From the perspective of the DSC lattice, $\bar{K}/\bar{H} = 0$ and $\bar{K}/\bar{H} = 1$ correspond to the case where the two oppositely-oriented DSC dislocations for each grain boundary lie directly atop each other causing them to annihilate, whereas $\bar{K}/\bar{H} = 0.5$ corresponds to the case where the two DSC dislocations are maximally separated by $\bar{H}/2$.

Fig. 5.3a,b shows how the kink energy and the barrier energy vary for different W and, therefore, the grain boundary spacing. The results show that beyond a cell width of ∼100 Å, the kink energy plateaus and becomes insensitive to W. This implies that the dominant contribution to the kink energy arises from kinks on the same grain boundary with minimal interactions between neighboring grain boundaries. The corresponding analysis for the cell height $\bar{H}$ is shown in Fig. 5.3c,d. Instead of a plateau, the kink energy profile increases monotonically with $\bar{H}$. The barrier energy exhibits a logarithmic dependence on H, as shown by plotting the migration barrier vs H in Fig. 5.3d. This is expected since grain boundary kinks are equivalent to DSC dislocations, and dislocation interaction energies exhibit a logarithmic dependence on their spacing [42]. The logarithmic dependence of the barrier energy on the cell height shows that the interaction energy of kinks from the same grain boundary is the dominant contribution to the energy given sufficiently large W so that neighboring grain boundaries do not interact. Having established the nature of finite size effects in our simulations, all subsequent energy profiles are produced for supercells with $W, \bar{H}$ so that the intra-grain boundary kink energy is dominant according to the analysis of Fig. 5.3.

Next, we consider the dependence of kink energy on grain boundaries with varying Σ. Fig. 5.4a,b shows the kink energy *vs.* $\bar{K}/\bar{H}$ for various Σ boundaries with $W = 120$ Å and $\bar{H} = 10$. In the atomistic model, we use $\bar{H}$ as

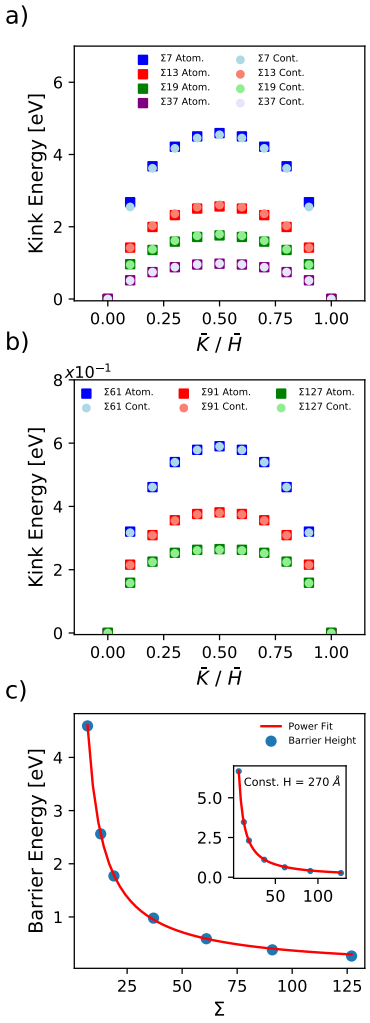

Figure 5.4: The grain boundary migration energy profiles for various grain boundaries with supercell $W = 120$Å, $\bar{H} = 6$ unit cell periods. (a, b) show the energy *vs.* $\bar{K}/\bar{H}$, the ratio of the grain boundary moved, for seven different Σ boundaries. Each boundary has its continuum energy superposed on its atomistic result. The maximum energy occurs at $\bar{K}/\bar{H} = 0.5$ corresponding to migrating half of the grain boundary. In the limit of large W, the value of the energy corresponds to the migration barrier energy of a grain boundary. (c) The atomistic grain boundary migration barrier energies are isolated to show the negative power-law relationship with Σ for constant $\bar{H}$. The inset shows the barrier energies for constant H=270 Å calculated with the continuum theory. The two graphs have the same trend, although the barrier energies are slightly larger for the inset (constant H) due to the logarithmic dependence on H.

opposed to H because the periodicity of the boundary, a_{CSL}, does not allow for a constant H across Σ. This is because a_{CSL} for each boundary is an irrational number, preventing any common factors. Therefore, the least common multiple is the product a_{CSL} from every considered boundary, which is too large for atomistic comparison. However, the continuum energy calculation for the DSC dislocations does not have this constraint. We show the effect of Σ on the barrier energy for constant H from the DSC framework in the inset of Fig. 5.4c, where the approximate cell height of the Σ127 boundary, H=270 Å, is used.

The energy profiles for high and low Σ boundaries are shown separately in Fig. 5.4a,b due to the order of magnitude difference in kink energies; the energy scale in Fig. 5.4b is smaller than the scale in Fig. 5.4a by an order of magnitude. Fig. 5.4c compares the energy barrier for each of the boundaries shown in 5.4a,b. Empirically we observe a power-law relationship in which the migration barrier scales as $\sim \Sigma^{-1}$. Low Σ boundaries have a higher migration barrier and are less mobile, while high Σ boundaries have a lower, nearly negligible migration barrier and so are more mobile. This is supported by the continuum energy calculation for constant H shown in the inset of Fig. 5.4c. Each DSC energy calculated in the inset is higher than its corresponding value in 5.4c. This is expected due to the result in Fig. 5.3d that shows a logarithmic relationship with H. We relate this to the observation that low (Σ7, Σ13) are most commonly seen after CVD growth [27], while other boundary angles anneal from the system [28, 33]. Using this understanding, coupled with the knowledge that dislocations anneal by merging with oppositely oriented dislocations, we posit that high Σ grain boundaries migrate and interact with other grain boundaries. If they have opposite sign, their dislocations can annihilate or, if they are of the same sign, the boundaries can continually merge until their dislocations are touching and form a more favorable Σ13 structure although not necessarily with θ_l=0 [27, 33].

5.3.2 Continuum Model

We now develop a continuum formulation to capture the atomistic trends shown in Figs. 5.3 and 5.4 using a description of kinked grain boundaries

as dislocations in the DSC lattice. Instead of explicitly considering the grain boundaries themselves, we consider only the kinks in the grain boundaries, which we have shown to be equivalent to DSC dislocations. For each double kinked boundary, there are two oppositely oriented DSC dislocations located a distance $\bar{K}$ apart (a DSC dislocation dipole). Each supercell, containing two double-kinked grain boundaries, can therefore be thought of as containing a DSC dislocation quadrupole. For a given configuration, the spacing of the DSC dislocations in the quadrupole depends on $\bar{H}$, W, and $\bar{K}$. Since the energy of grain boundary kinks is sensitive to the supercell dimensions, shown in Fig. 5.3, we choose a continuum model that naturally incorporates image interactions to capture any long-range interaction of the DSC dislocations.

To find the energy associated with the presence of the DSC dislocation quadrupole, we use a continuum formulation for the energy of a set of dislocations in a linear elastic medium that naturally incorporates periodic boundary conditions and accounts for dislocation-dislocation interactions. In this formulation, each dislocation introduces a topological constraint to the continuum distortion field

$$\epsilon_{kl}\partial_k \Delta_{lm} = \alpha_m \tag{5.1}$$

where the curl of the distortion field (Δ) must equal the Nye tensor (α), the density of dislocations. The Nye tensor, α_m, for a dislocation centered at the origin is given by

$$\alpha_m(\vec{r}) = b_m \delta(\vec{r}) \tag{5.2}$$

where b_m is the m^{th} component of the Burgers vector of the dislocation and δ is the Kronecker-delta function. However, the singularity of the delta function in Eq. 5.2 is sufficient to cause the total energy of the dislocation to diverge. The divergence can be avoided by smearing the delta function into a gaussian according to

$$\alpha_m(\vec{r}) = b_m \exp\left(-\frac{\vec{r}^2}{R_{DSC}^2}\right) , \tag{5.3}$$

where R_{DSC} is the gaussian effective width and defined as the DSC dislocation core radius, the single adjustable parameter of our model.

To account for the periodic boundary conditions and the resulting image

interactions between dislocations in neighboring supercells, we write the distortion tensor as a sum over Fourier components $\widetilde{\Delta}$ according to

$$\Delta_{ij}\big(\vec{X}\big) = \sum_{\vec{G}} \widetilde{\Delta}_{ij}\big(\vec{G}\big) \exp[i\vec{G}\cdot\vec{X}] \tag{5.4}$$

where $\vec{G}$ represents the reciprocal lattice (wave) vectors. The total distortion energy, E_d, associated with the distortion field is then given by

$$\begin{aligned} E_d &= \frac{1}{2} C_{jklm} \int_{cell} \Delta_{jk}\Delta^*_{lm} dA \\ &= \frac{1}{2}\Omega_c C_{jklm} \sum_{\vec{G}} \widetilde{\Delta}_{jk}\widetilde{\Delta}^*_{lm} \end{aligned} \tag{5.5}$$

where C_{jklm} are the components of the fourth order elastic stiffness tensor as determined by the interatomic potential used, and Ω_c is the supercell area.

By substituting Eqs. 5.3 and 5.4 into Eq. 5.1, a linear set of equations relating the Fourier components $\widetilde{\Delta}$ for each $\vec{G}$ is obtained. However, the topological constraints of Eq. 5.1 do not uniquely determine the distortion tensor. The actual total distortion field that exists in the system is the one that satisfies all topological constraints associated with the dislocations present but uses all remaining degrees of freedom to minimize the total distortion energy in Eq. 5.5. The energy can be minimized separately for each $\vec{G}$ component (as they are linearly independent). Once the components $\widetilde{\Delta}$ are obtained, the energy terms are summed to find the total distortion energy. This approach has been applied previously to describe the energetics of 5–7 (real space) dislocations in two-dimensional materials [25], but to our knowledge this is the first application to dislocations in the DSC lattice to describe grain boundary kinks.

The best-fit core radius, R_{DSC}, for the DSC dislocations is determined independently for each Σ grain boundary considered *via* a least squares fit of the continuum model to the atomistic results sampling across different $\bar{H}$, W, and $\bar{K}$. Fig. 5.4a,b compares the atomistic migration energies to those calculated by the model using the best fit R_{DSC}. Further, the continuum results are plotted on top of atomistic energies shown in Fig. 5.3 to show the agreement between the DSC framework and the atomistic results. The continuum approach captures all the trends of the atomistic simulations over

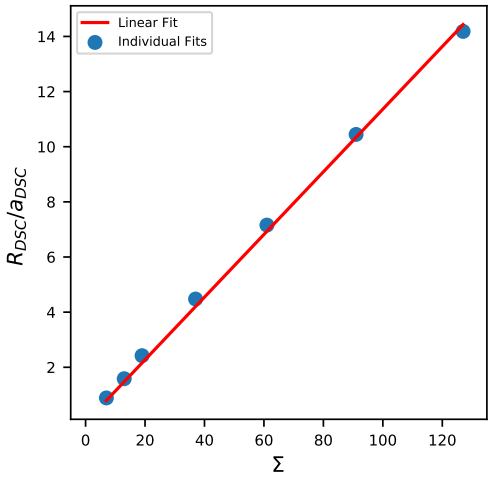

Figure 5.5: The ratio of the DSC dislocation core radius, R_{DSC}, to the DSC lattice spacing, a_{DSC}, exhibits a near-linear dependence with Σ. The linear relationship shows that the core radius is constant with respect to the CSL spacing, a_{CSL}, which itself is linearly related to a_{DSC}.

the full range of Σ values and supercell dimensions. For all cases considered, the maximum discrepancy between the continuum and atomistic framework is less than 2%. The agreement between the atomistic and continuum curves show that, in essence, grain boundary kinks interact with each other elastically in a manner analogous to the interactions of linear elastic dislocations in the real crystal lattice. Surprisingly, this interaction is captured through modeling grain boundary kinks as dislocations in the topological DSC lattice that does not capture all the atomic sites of graphene.

5.4 Implications of Equivalence

Since grain boundary kinks can be interpreted as dislocations, we reinterpret the atomistic results with our continuum framework and dislocation theory. Fig. 5.5 shows the best-fit core radius normalized by the DSC dislocation Burgers vector, $R_s = R_{DSC}/a_{DSC}$, as a function of Σ, revealing a linear relationship. Since the ratio between the CSL and DSC lattice vectors is also linear with Σ, the ratio of the core radius to the CSL lattice vector is constant across all Σ. We believe this to be a general result for boundaries described using CSL/DSC theory because the normalization parameter a_{CSL}

is a topological descriptor of the system. Using the linear relationship, we can reduce the free parameters in our model to just one. Rather than one core radius for each type of grain boundary, only one parameter, the slope of Fig. 5.5, is sufficient to define all core radii and, ultimately, the energetics of all grain boundary kinks in graphene. Numerically, for a given Σ boundary in graphene we obtain $R_{DSC} = 0.11\Sigma a_{DSC} = 0.11 a_{CSL}$, where 0.11 is the slope in Fig. 5.5.

We can also return to Fig. 5.4c to analyze the Σ^{-1} power-law dependence of the migration barriers in light of grain boundary kinks obeying the linear elastic theory of dislocations. According to linear elasticity theory, the total energy of a dislocation scales as b^2, the square of the magnitude of the burgers vector [42]. The magnitude of the Burgers vector of DSC dislocations is given by the DSC lattice spacing, which varies according to $\Sigma^{-1/2}$. Therefore, a Σ^{-1} dependence naturally arises. The agreement between our results and the standard, linear elastic interaction energy of dislocations further shows the correspondence between graphene grain boundary kinks and dislocations in the DSC lattice.

CHAPTER 6

CONCLUSIONS

To conclude, we have shown that grain boundary kinks in graphene are equivalent to DSC dislocations. This allows us to understand grain boundary structure and motion using the linear elastic theory of dislocations. Our atomistic simulations show that grain boundary migration barriers have a negative power-law dependence with Σ. The power-law relationship is attributed to the dependence of the DSC dislocation's Burgers vector on Σ for each boundary. The lower energy barrier of high Σ boundaries is posited to explain why only low Σ are found in annealed graphene polycrystals from experiments and simulations. The continuum analysis is unified across all boundaries by showing that the single fitting parameter, R_{DSC}, is constant with respect to the CSL spacing. The unification of the theory allows grain boundary kinks to be interpreted using the linear elastic theory of dislocations. This result allows us to interpret grain boundary motion in graphene as dislocation movement, which provides insight to engineer defects in graphene and tune its properties.

CHAPTER 7

FUTURE WORK

Having completed this work, there are two avenues that may be useful to pursue. One is to continue thinking of grain boundaries as tools to tailor the properties of graphene. The other is to develop additional topological analysis methods to analyze 2D materials and their heterostructures.

7.1 Graphene Grain Boundary Functionalization

The analysis of the dislocation nature of grain boundary kinks opens a few possibilities for further research. This work looks at the thermodynamics of grain boundary migration; kinks are imposed by bond rotations and the equilibrium energy is found. This assumes that grain boundary motion follows a reaction pathway, artificially (although logically) choosing the reaction steps.

Although bond rotations correctly transform the structure, it is not accomplished by a physical process. In 3D materials, grain boundary motion naturally occurs as a result of an applied shear strain. Homer *et al.* cataloged 388 different grain boundaries and investigated their shear-coupled nature [43]. They found that the coupling constants agreed well with theory, but that their mobility was inversely related with coupling. Applying shear will provide a physical method to migrate grain boundaries in simulation and in experiment.

We can then look at different Σ boundaries to characterize their response to shear stress. This can be used to look at the dynamic mobility of grain boundaries. The use of applied shear, instead of bond rotations, provides a method to look at the energetics of grain boundary motion through a physical lens. Where bond rotations give minimum energy steps, shear could illuminate energy barriers that might exist between these positions.

7.2 CSL/DSC Analysis of 2D materials

Alternatively, topological analysis methods can be expanded to understand the role of the basis atoms of graphene and how they can be used to analyze 2D bilayers. Since graphene is made entirely of carbon, the basis atom could add partial dislocations to the DSC lattice that would allow for more shifts to the grain boundary. This was not considered in this work as we primarily looked at grain boundaries with 5-7 dislocations, which only operate on one sub-lattice. However, it is possible that grain boundaries composed of other disclinations have DSC dislocations that show partial dislocations. An example boundary could be the 8 atom disclination and two 5 atom disclinations labeled as an 855 grain boundary. This grain boundary separates two anti-phase grains with $\theta_m \sim 30^\circ$

Another possibility is to apply CSL/DSC theory to stacked 2D material systems. Since CSL theory was developed to analyze dichromatic patterns of bicrystals, it should be transferable to other stacking systems such as 2D heterostructures. Layered 2D materials provide an avenue to further tailor the properties of devices as they provide atomic interfaces, a novel feature in device fabrication. The degree to which 2D material properties change when put into a layered structure depends on the interlayer coupling, which is dependent on the CSL of the bilayers. Since CSL/DSC theory analyzes the commensurate nature of bilayers, it is possible that CSL/DSC theory could be used to predict structures with a desired property. For example, the topology of the "magic angles" that resulted in superconductivity of bilayer graphene could be analyzed to see if there are other such angles [13].

REFERENCES

[1] M. J. Allen, V. C. Tung, and R. B. Kaner, "Honeycomb carbon: A review of graphene," *Chemical Reviews*, vol. 110, no. 1, pp. 132–145, 01 2010. [Online]. Available: https://doi.org/10.1021/cr900070d

[2] K. S. Novoselov, D. Jiang, F. Schedin, T. J. Booth, V. V. Khotkevich, S. V. Morozov, and A. K. Geim, "Two-dimensional atomic crystals," *Proceedings of the National Academy of Sciences*, vol. 102, no. 30, pp. 10 451–10 453, 2005. [Online]. Available: http://www.pnas.org/content/102/30/10451

[3] A. K. Geim and I. V. Grigorieva, "Van der waals heterostructures," *Nature*, vol. 499, pp. 419 EP –, 07 2013. [Online]. Available: http://dx.doi.org/10.1038/nature12385

[4] O. Minoru and S. Takayoshi, "Two-dimensional dielectric nanosheets: Novel nanoelectronics from nanocrystal building blocks," *Advanced Materials*, vol. 24, no. 2, pp. 210–228. [Online]. Available: https://onlinelibrary.wiley.com/doi/abs/10.1002/adma.201103241

[5] J. K. Ellis, M. J. Lucero, and G. E. Scuseria, "The indirect to direct band gap transition in multilayered mos2 as predicted by screened hybrid density functional theory," *Applied Physics Letters*, vol. 99, no. 26, p. 261908, 2011. [Online]. Available: https://doi.org/10.1063/1.3672219

[6] K. S. Novoselov, A. Mishchenko, A. Carvalho, and A. H. Castro Neto, "2d materials and van der waals heterostructures," *Science*, vol. 353, no. 6298, 2016. [Online]. Available: http://science.sciencemag.org/content/353/6298/aac9439

[7] Y. Ein-Eli, B. Markovsky, D. Aurbach, Y. Carmeli, H. Yamin, and S. Luski, "The dependence of the performance of li-c intercalation anodes for li-ion secondary batteries on the electrolyte solution composition," *Electrochimica Acta*, vol. 39, no. 17, pp. 2559 – 2569, 1994. [Online]. Available: http://www.sciencedirect.com/science/article/pii/0013468694002215

[8] A. Gupta, T. Sakthivel, and S. Seal, "Recent development in 2d materials beyond graphene," *Progress in Materials Science*, vol. 73, pp. 44 – 126, 2015. [Online]. Available: http://www.sciencedirect.com/science/article/pii/S0079642515000237

[9] P. San-Jose, J. González, and F. Guinea, "Electron-induced rippling in graphene," *Phys. Rev. Lett.*, vol. 106, p. 045502, Jan 2011. [Online]. Available: https://link.aps.org/doi/10.1103/PhysRevLett.106.045502

[10] K. S. Novoselov, A. K. Geim, S. V. Morozov, D. Jiang, M. I. Katsnelson, I. V. Grigorieva, S. V. Dubonos, and A. A. Firsov, "Two-dimensional gas of massless dirac fermions in graphene," *Nature*, vol. 438, pp. 197 EP –, 11 2005. [Online]. Available: http://dx.doi.org/10.1038/nature04233

[11] K. I. Bolotin, F. Ghahari, M. D. Shulman, H. L. Stormer, and P. Kim, "Observation of the fractional quantum hall effect in graphene," *Nature*, vol. 462, pp. 196 EP –, 11 2009. [Online]. Available: http://dx.doi.org/10.1038/nature08582

[12] A. S. Mayorov, R. V. Gorbachev, S. V. Morozov, L. Britnell, R. Jalil, L. A. Ponomarenko, P. Blake, K. S. Novoselov, K. Watanabe, T. Taniguchi, and A. K. Geim, "Micrometer-scale ballistic transport in encapsulated graphene at room temperature," *Nano Letters*, vol. 11, no. 6, pp. 2396–2399, 06 2011. [Online]. Available: https://doi.org/10.1021/nl200758b

[13] Y. Cao, V. Fatemi, S. Fang, K. Watanabe, T. Taniguchi, E. Kaxiras, and P. Jarillo-Herrero, "Unconventional superconductivity in magic-angle graphene superlattices," *Nature*, vol. 556, pp. 43 EP –, 03 2018. [Online]. Available: http://dx.doi.org/10.1038/nature26160

[14] A. Maffucci and G. Miano, "Electrical properties of graphene for interconnect applications," vol. 4, pp. 305–317, 06 2014.

[15] C. Lee, X. Wei, J. W. Kysar, and J. Hone, "Measurement of the elastic properties and intrinsic strength of monolayer graphene," *Science*, vol. 321, no. 5887, pp. 385–388, 2008. [Online]. Available: http://science.sciencemag.org/content/321/5887/385

[16] K. H. Kim, Y. Oh, and M. F. Islam, "Graphene coating makes carbon nanotube aerogels superelastic and resistant to fatigue," *Nature Nanotechnology*, vol. 7, pp. 562 EP –, 07 2012. [Online]. Available: http://dx.doi.org/10.1038/nnano.2012.118

[17] L. A. Falkovsky, "Optical properties of graphene," *Journal of Physics: Conference Series*, vol. 129, no. 1, p. 012004, 2008. [Online]. Available: http://stacks.iop.org/1742-6596/129/i=1/a=012004

[18] S. Diao, X. Zhang, Z. Shao, K. Ding, J. Jie, and X. Zhang, "12.35graphene quantum dots/silicon heterojunction solar cells using graphene transparent electrode," *Nano Energy*, vol. 31, pp. 359 – 366, 2017. [Online]. Available: http://www.sciencedirect.com/science/article/pii/S2211285516305468

[19] S. Bae, H. Kim, Y. Lee, X. Xu, J.-S. Park, Y. Zheng, J. Balakrishnan, T. Lei, H. Ri Kim, Y. I. Song, Y.-J. Kim, K. S. Kim, B. Özyilmaz, J.-H. Ahn, B. H. Hong, and S. Iijima, "Roll-to-roll production of 30-inch graphene films for transparent electrodes," *Nature Nanotechnology*, vol. 5, pp. 574 EP –, 06 2010. [Online]. Available: http://dx.doi.org/10.1038/nnano.2010.132

[20] T. Kobayashi, M. Bando, N. Kimura, K. Shimizu, K. Kadono, N. Umezu, K. Miyahara, S. Hayazaki, S. Nagai, Y. Mizuguchi, Y. Murakami, and D. Hobara, "Production of a 100-m-long high-quality graphene transparent conductive film by roll-to-roll chemical vapor deposition and transfer process," *Applied Physics Letters*, vol. 102, no. 2, p. 023112, 2013. [Online]. Available: https://doi.org/10.1063/1.4776707

[21] Y. Wei, J. Wu, H. Yin, X. Shi, R. Yang, and M. Dresselhaus, "The nature of strength enhancement and weakening by pentagon–heptagon defects in graphene," *Nature Materials*, vol. 11, pp. 759 EP –, 07 2012. [Online]. Available: http://dx.doi.org/10.1038/nmat3370

[22] A. W. Tsen, L. Brown, M. P. Levendorf, F. Ghahari, P. Y. Huang, R. W. Havener, C. S. Ruiz-Vargas, D. A. Muller, P. Kim, and J. Park, "Tailoring electrical transport across grain boundaries in polycrystalline graphene," *Science*, vol. 336, no. 6085, pp. 1143–1146, 2012. [Online]. Available: http://science.sciencemag.org/content/336/6085/1143

[23] A. Carpio, L. L. Bonilla, F. de Juan, and M. A. H. Vozmediano, "Dislocations in graphene," *New Journal of Physics*, vol. 10, no. 5, p. 053021, 2008. [Online]. Available: http://stacks.iop.org/1367-2630/10/i=5/a=053021

[24] O. V. Yazyev and S. G. Louie, "Topological defects in graphene: Dislocations and grain boundaries," *Phys. Rev. B*, vol. 81, p. 195420, May 2010. [Online]. Available: https://link.aps.org/doi/10.1103/PhysRevB.81.195420

[25] E. Ertekin, D. C. Chrzan, and M. S. Daw, "Topological description of the stone-wales defect formation energy in carbon nanotubes and graphene," *Phys. Rev. B*, vol. 79, p. 155421, Apr 2009. [Online]. Available: https://link.aps.org/doi/10.1103/PhysRevB.79.155421

[26] E. Cockayne, G. M. Rutter, N. P. Guisinger, J. N. Crain, P. N. First, and J. A. Stroscio, "Grain boundary loops in graphene," *Phys. Rev. B*, vol. 83, p. 195425, May 2011. [Online]. Available: https://link.aps.org/doi/10.1103/PhysRevB.83.195425

[27] C. Ophus, A. Shekhawat, H. Rasool, and A. Zettl, "Large-scale experimental and theoretical study of graphene grain boundary structures," *Phys. Rev. B*, vol. 92, p. 205402, Nov 2015. [Online]. Available: https://link.aps.org/doi/10.1103/PhysRevB.92.205402

[28] J. Zhuang, R. Zhao, J. Dong, T. Yan, and F. Ding, "Evolution of domains and grain boundaries in graphene: a kinetic monte carlo simulation," *Phys. Chem. Chem. Phys.*, vol. 18, pp. 2932–2939, 2016. [Online]. Available: http://dx.doi.org/10.1039/C5CP07142A

[29] Q. Du, V. Faber, and M. Gunzburger, "Centroidal voronoi tessellations: Applications and algorithms," *SIAM Review*, vol. 41, no. 4, pp. 637–676, 1999. [Online]. Available: https://doi.org/10.1137/S0036144599352836

[30] A. Shekhawat, C. Ophus, and R. O. Ritchie, "A generalized read-shockley model and large scale simulations for the energy and structure of graphene grain boundaries," *RSC Adv.*, vol. 6, pp. 44 489–44 497, 2016. [Online]. Available: http://dx.doi.org/10.1039/C6RA07584C

[31] J. Hirth, R. Pond, R. Hoagland, X.-Y. Liu, and J. Wang, "Interface defects, reference spaces and the frankÃćÂĂÂŞbilby equation," *Progress in Materials Science*, vol. 58, no. 5, pp. 749 – 823, 2013. [Online]. Available: http://www.sciencedirect.com/science/article/pii/S0079642512000746

[32] W. T. Reynolds, *Interfaces in Crystalline Materials By A. P. Sutton (University of Oxford) and R. W. Balluffi (MIT). Oxford University Press: New York. 1995. xxvii + 819 pp. $165. ISBN 0-19-851385-2.* American Chemical Society, 03 1997, vol. 119, no. 9. [Online]. Available: https://doi.org/10.1021/ja955377x

[33] A. V. Tyurnina, H. Okuno, P. Pochet, and J. Dijon, "Cvd graphene recrystallization as a new route to tune graphene structure and properties," *Carbon*, vol. 102, pp. 499 – 505, 2016. [Online]. Available: http://www.sciencedirect.com/science/article/pii/S0008622316301865

[34] T. I. Mazilova, V. A. Ksenofontov, V. Voyevodin, E. V. Sadanov, and I. Mikhailovskij, "Mechanical recrystallization of ultra-strength tungsten nanoneedles," vol. 91, pp. 304–312, 04 2011.

[35] D. Warrington and P. Bufalini, "The coincidence site lattice and grain boundaries," *Scripta Metallurgica*, vol. 5, no. 9, pp. 771 – 776, 1971. [Online]. Available: http://www.sciencedirect.com/science/article/pii/003697487190161X

[36] WARRINGTON, D. H., "The coincidence site lattice (csl) and grain boundary (dsc) dislocations for the hexagonal lattice," *J. Phys. Colloques*, vol. 36, pp. C4–87–C4–95, 1975. [Online]. Available: https://doi.org/10.1051/jphyscol:1975410

[37] W. Bollmann, *Crystal defects and crystalline interfaces*. Springer, 1970.

[38] and, "The symmetry and interfacial structure of bicrystals," *Philosophical Transactions of the Royal Society of London A: Mathematical, Physical and Engineering Sciences*, vol. 292, no. 1395, pp. 449–472, 1979. [Online]. Available: http://rsta.royalsocietypublishing.org/content/292/1395/449

[39] http://lammps.sandia.gov.

[40] S. Plimpton, "Fast parallel algorithms for short-range molecular dynamics," *Journal of Computational Physics*, vol. 117, no. 1, pp. 1 – 19, 1995. [Online]. Available: http://www.sciencedirect.com/science/article/pii/S002199918571039X

[41] L. Lindsay and D. A. Broido, "Optimized tersoff and brenner empirical potential parameters for lattice dynamics and phonon thermal transport in carbon nanotubes and graphene," *Phys. Rev. B*, vol. 81, p. 205441, May 2010. [Online]. Available: https://link.aps.org/doi/10.1103/PhysRevB.81.205441

[42] J. Hirth and J. Lothe, *Theory of Dislocations*. Malabar, Florida: Krieger Publishing Company, 1992.

[43] E. R. Homer, S. M. Foiles, E. A. Holm, and D. L. Olmsted, "Phenomenology of shear-coupled grain boundary motion in symmetric tilt and general grain boundaries," *Acta Materialia*, vol. 61, no. 4, pp. 1048 – 1060, 2013. [Online]. Available: http://www.sciencedirect.com/science/article/pii/S1359645412007306